cmgh
CELLULAR AND MOLECULAR GASTROENTEROLOGY AND HEPATOLOGY

ORIGINAL RESEARCH

CDKN2A-p16 Deletion and Activated KRAS^{G12D} Drive Barrett's-Like Gland Hyperplasia-Metaplasia and Synergize in the Development of Dysplasia Precancer Lesions

Jing Sun,[1] Jorge L. Sepulveda,[1] Elena V. Komissarova,[1] Caitlin Hills,[1] Tyler D. Seckar,[1] Narine M. LeFevre,[2] Hayk Simonyan,[1] Colin Young,[2] Gloria Su,[3] Armando Del Portillo,[3] Timothy C. Wang,[4] and Antonia R. Sepulveda[1]

[1]*Department of Pathology, George Washington University School of Medicine and Health Sciences, Washington, DC;* [2]*Department of Pharmacology & Physiology, George Washington University, School of Medicine and Health Sciences, Washington, DC;* [3]*Department of Pathology and Cell Biology, Columbia University, New York, New York; and* [4]*Division of Digestive and Liver diseases, Department of Medicine, Columbia University, New York, New York*

SUMMARY

CDKN2A-p16 deletion in LGR5$^+$ stem cell progenitors in the stomach squamocolumnar junction triggers increased mucous-gland hyperplasia/metaplasia. Oncogenic KRAS^{G12D} synergizes with p16-deletion resulting in higher-grades of glandular dysplasia, supporting a functional role of p16 and KRAS in the progression of Barrett's-like lesions to dysplasia.

BACKGROUND & AIMS: Barrett's esophagus is the precursor of esophageal dysplasia and esophageal adenocarcinoma. CDKN2A-p16 deletions were reported in 34%–74% of patients with Barrett's esophagus who progressed to dysplasia and esophageal adenocarcinoma, suggesting that p16 loss may drive neoplastic progression. KRAS activation frequently occurs in esophageal adenocarcinoma and precancer lesions. LGR5$^+$ stem cells in the squamocolumnar-junction (SCJ) of mouse stomach contribute as Barrett's esophagus progenitors. We aimed to determine the functional effects of p16 loss and KRAS activation in Barrett's-like metaplasia and dysplasia development.

METHODS: We established mouse models with conditional knockout of CDKN2A-p16 (p16KO) and/or activated KRAS^{G12D} expression targeting SCJ LGR5$^+$ cells in interleukin 1b transgenic mice and characterized histologic alterations (mucous-gland hyperplasia/metaplasia, inflammation, and dysplasia) in mouse SCJ. Gene expression was determined by microarray, RNA sequencing, and immunohistochemistry of SCJ tissues and cultured 3-dimensional organoids.

RESULTS: p16KO mice exhibited increased mucous-gland hyperplasia/metaplasia versus control mice ($P = .0051$). Combined p16KO+KRAS^{G12D} resulted in more frequent dysplasia and higher dysplasia scores ($P = .0036$), with 82% of p16KO+KRAS^{G12D} mice developing high-grade dysplasia. SCJ transcriptome analysis showed several activated pathways in p16KO versus control mice (apoptosis, tumor necrosis factor-α/nuclear factor-kB, proteasome degradation, p53 signaling, MAPK, KRAS, and G1-to-S transition).

CONCLUSIONS: p16 deletion in LGR5$^+$ cell precursors triggers increased SCJ mucous-gland hyperplasia/metaplasia. KRAS^{G12D} synergizes with p16 deletion resulting in higher grades of SCJ glandular dysplasia, mimicking Barrett's high-grade dysplasia. These genetically modified mouse models establish a functional role of p16 and activated KRAS in the progression of Barrett's-like lesions to dysplasia in mice, representing an *in vivo* model of esophageal adenocarcinoma precancer. Derived 3-dimensional organoid models further provide *in vitro* modeling opportunities of esophageal precancer stages. *(Cell Mol Gastroenterol Hepatol 2024;17:769–784; https://doi.org/10.1016/j.jcmgh.2024.01.014)*

Keywords: Barrett's metaplasia, CDKN2A-p16, KRAS, Dysplasia, Esophageal adenocarcinoma, Murine genetic models, 3D organoids, Transcriptomics.

The molecular mechanisms that drive transformation of the normal lining of the esophagus into Barrett's esophagus (BE) metaplasia and dysplasia, the precursor lesions of esophageal adenocarcinoma (EAC), have been explored at the genomic level, revealing alternative driver pathways and combinations of alterations that arise early in precancer metaplastic lesions.[1–3] However, molecular biomarker testing of BE tissues taken during BE surveillance remains mostly limited to research protocols, indicating that better understanding of cellular and molecular alterations is warranted.[4,5] EAC incidence has continued to rise for the past 4 decades in western countries.[4,5]

Abbreviations used in this paper: **3D, 3-dimensional; BA, bile acid; BE, Barrett's esophagus; CI, confidence interval; EAC, esophageal adenocarcinoma; FDR, false discovery rate; IL1b, interleukin 1 beta; MAPK, mitogen activated protein kinases; RNASeq, RNA sequencing; SCJ, squamocolumnar-junction; scRNASeq, single-cell RNASeq; UMAP, uniform manifold approximation and projection.**

Most current article

2352-345X
https://doi.org/10.1016/j.jcmgh.2024.01.014

The interleukin 1 beta (IL1b) transgenic mouse model that reproduces human BE, dysplasia, and adenocarcinoma sequence of alterations provides a tool to decipher the roles of distinct molecular drivers from early metaplastic lesions to advanced dysplasia/EAC.[6] In these mice, development of BE, dysplasia, and EAC was accelerated by exposure to bile acids (BA) and/or nitrosamines and was inhibited by IL6 deficiency. Kunze et al[7] reported that Lgr5^{+} gastric cardia stem cells present in BE were able to lineage trace the early BE lesion, suggesting that BE and EAC arise from gastric progenitors caused by a tumor-promoting IL1β/IL6 signaling cascade and DLL1-dependent Notch signaling. Stachler et al[8] reported 2 main pathways of progression from Barrett's metaplasia to dysplasia and EAC, 1 involving early loss of CDKN2A and the other inactivation of TP53 and genome doubling. Our published studies showed that CDKN2A-p16 inactivation occurred in 69% of patients with Barrett's metaplasia 1 or more years before development of dysplasia and/or adenocarcinoma, versus 21% of patients with Barrett's metaplasia who did not progress to dysplasia or EAC.[3] However, how p16 may promote esophageal metaplastic precancer lesions and enhance the risk of dysplasia has not been modeled or demonstrated by functional *in vivo* studies.

CDKN2A-p16 (p16) is a member of the INK4 family of cyclin-dependent kinase inhibitor proteins that negatively regulate progression through the G_1 phase of the cell cycle by binding to and inhibiting cyclin D/CDK4-6 complexes.[9] Inactivation of p16 confers increased susceptibility to many human malignancies, including pancreatic, esophageal, and other carcinomas.[10–12] P16 inactivation has been reported to occur frequently not only in EAC, but also in preneoplastic BE metaplasia and dysplastic precursor lesions.[3,11–15] In addition, p16 has been shown to play key roles in cellular senescence and aging.[16] Oncogenic KRAS driven cancer was shown to require ablation of p16 to overcome oncogene-associated senescence in a mouse model of pancreas cancer.[17] Despite these advances, a mechanistic understanding using *in vivo* models of stepwise esophageal carcinogenesis driven by loss of p16 and KRAS activation has not been reported.

Here, we leverage conditional Lgr5^{+} cell lineage p16 knockout (p16KO) and knock-in (KRAS^{G12D}) to advance the understanding of the roles of p16 and oncogenic KRAS in the development of esophageal mucous gland hyperplasia/metaplasia and dysplasia in the IL1b mouse model. Furthermore, we performed transcriptome analysis of genes and pathways affected by p16KO in comparison with p16 wild-type (p16WT) squamocolumnar junction (SCJ) mucous gland tissue samples and from established 3-dimensional (3D) organoids to model the molecular landscape that occurs in the BE precancer as a consequence of p16 inactivation. These 3D organoid *in vitro* models may be useful for future manipulation of their genetic makeup to replicate multiple genomic landscapes of esophageal precancer.

Results

Mucous Gland Hyperplasia-Metaplasia, Dysplasia, and Inflammation in the Squamocolumnar Junction of Mouse Stomachs With CDKN2A-p16 Deletion in LGR5-Progenitor-Derived Cells

In this study we first tested the hypothesis that p16 loss in LGR5-progenitor derived cells contributes to hyperplasia-metaplasia and may enhance dysplasia in the cardia-type mucous gland metaplasia in a mouse model. In this phase of the study, we induced conditional CDKN2A-p16 deletion targeted to LGR5-expressing progenitor cells to generate p16KO mice (*Lgr5-Cre*$^{+/-}$*; IL1B*^{tg}*; p16*$^{flox/flox}$) after tamoxifen injection at 6–8 weeks every 48 hours for a total of 3 injections and compared with control (p16WT: *Lgr5-Cre*$^{+/-}$*; IL1B*^{tg}*; p16*$^{wt/wt}$) mice. All mice expressed the *IL1B* transgene and were treated with oral deoxycholate, previously reported to be a model of Barrett's-like lesions in the mouse SCJ.[6]

Examination of open mouse stomachs showed that SCJ of p16KO mice was associated with thickened SCJ with enhanced nodular appearance (Figure 1*A* and *B*). Mucous gland hyperplasia/metaplasia in the SCJ of p16KO mice was associated with thickened SCJ with enhanced nodular appearance (Figure 1). SCJ histology was examined on hematoxylin and eosin–stained sections revealing that the SCJ of p16KO mice exhibited larger areas of hyperplastic/metaplastic cardia-type mucous glands compared with p16WT mice, showing more complex architecture with higher numbers of mucous glands, often emerging from individual mucous/cardia-like gland units (Figure 1*E* and *F*). In mice carrying the *ROSA26-tdTomato/RFP* gene, tamoxifen treatment resulted in expression of tdRFP as a marker of Lgr5-Cre-induced recombination in SCJ glands derived from LGR5^{+} progenitor cells (Figure 1*J-L*). P16KO mice exhibited reduced expression of p16 in cardia-type mucous glands compared with p16WT mice, by immunohistochemistry for p16 protein expression (Figure 1*M* and *N*).

Overall, median SCJ mucous gland numbers were significantly higher in the p16KO mice (13.0) as compared with p16WT mice (8.0) ($P = .0051$) (Figure 2*A*). P16KO mice of age groups 4, 9, and 15 months showed higher scores of mucous gland hyperplasia/metaplasia than p16WT, but the difference only reached significance ($P = .029$) for mice in the 9-month age group (Figure 2*A*). Ki67 expression quantified by quantitative multispectral immunofluorescence showed increased proliferation in cardia-type glands at the SCJ of p16KO as compared with p16WT mice performed in representative mice at age 9 months (Figure 1*O-Q*; $P = .042$).

Overall, 46% of p16WT mice had no gland dysplasia compared with 23% of p16KO mice, and grade 2 dysplasia was only noted in the p16KO group (Figure 2*B*). Although mice with p16KO had higher dysplasia scores, this did not reach statistical significance ($P = .14$; Figure 2*B*), and no

significant differences in dysplasia were seen at 4, 9, or 15 months ($P = .49$, $P = .20$, and $P = .37$, respectively).

Overall, p16KO mice had higher inflammation scores versus p16WT mice, with 100% of p16KO mice showing inflammation scores of 2 or 3, whereas only 70% of p16WT mice had inflammation scores of 2 or 3 (Figure 2*C*); however, this did not reach statistical significance ($P = .053$), and no significant differences in inflammation were seen at 4, 9, or 15 months ($P = .21$, $P = .14$, and $P = 1$), respectively. There was a positive correlation between inflammation and hyperplasia/metaplasia ($R = .44$, $P = .026$; Figure 2*D*).

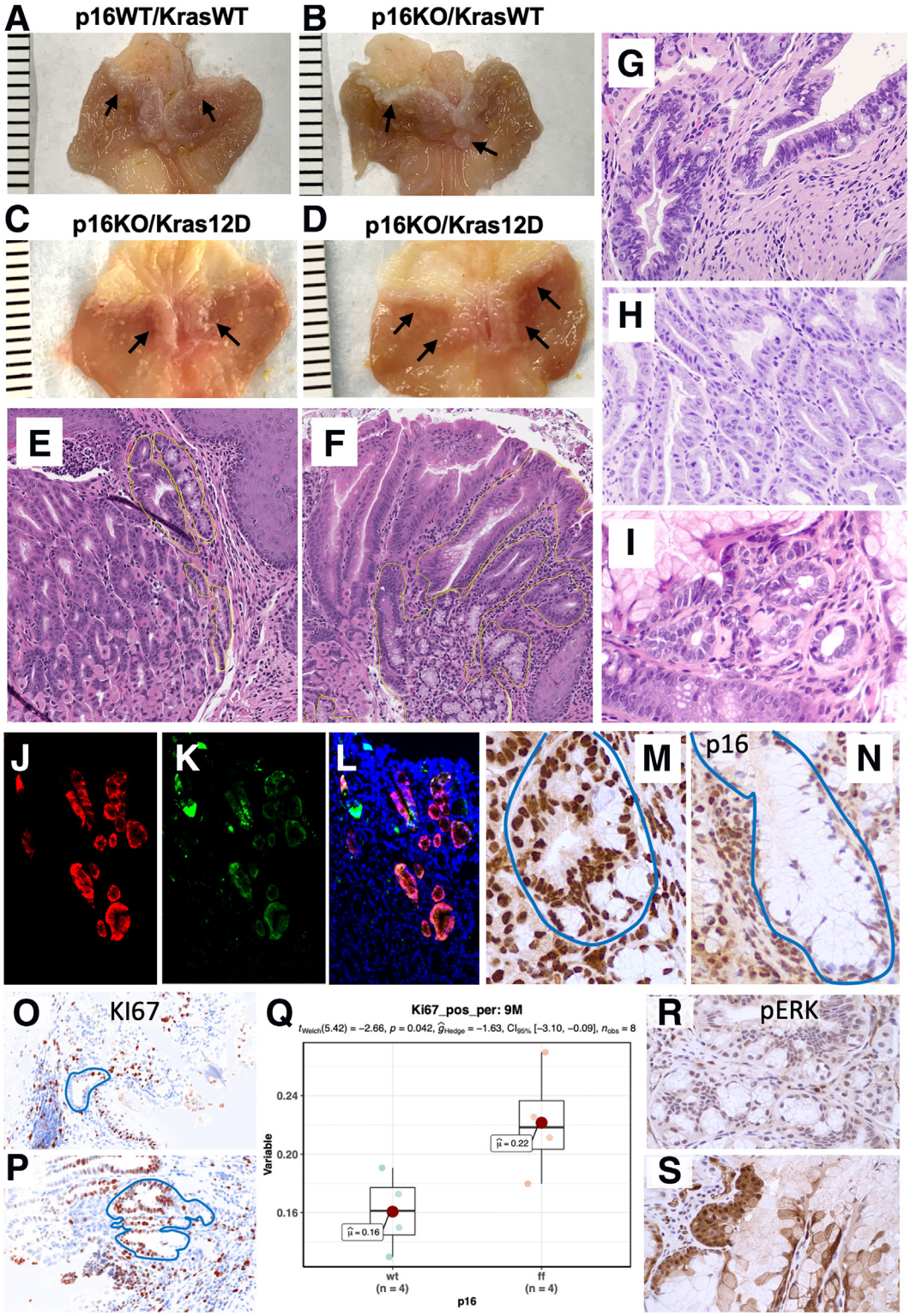

In addition to analysis of proportions, we performed ordinal logistic regression, which does not depend on balanced numbers of mice in each age group, on a set of 23 p16WT and 22 p16KO mice of ages ranging from 3.6 to 22 months, and showed that the deletion of p16 is associated with a 2.62 (confidence interval [CI], 1.41–3.97) increase in gland hyperplasia-metaplasia ($P = 5.3e-5$), 2.05 (CI, 0.7–3.68) increase in inflammation ($P = .0055$), and 2.11 (CI, 0.75–3.67) increase in dysplasia ($P = .0042$). Hyperplasia-metaplasia and dysplasia increased with age in both groups: for each month of age, there was a 0.18 (CI, 0.08–0.29) increase in gland hyperplasia-metaplasia ($P = .00086$) and a 0.33 (CI, 0.19–0.51) increase in dysplasia ($P = 4.7e-05$).

$KRAS^{G12D}$ Synergizes With CDKN2A-p16 Deletion in LGR5-Derived Cells Enhancing Glandular Dysplasia in the Mouse Stomach Squamocolumnar Junction

Given our observation that p16KO in the IL1b driven inflammation field was not sufficient to significantly enhance dysplasia in SCJ cardia-type glandular epithelium in age-matched mice up to 15 months, we tested whether $KRAS^{G12D}$ activation alone or in combination with p16 deletion would affect SCJ gland dysplasia, hyperplasia/metaplasia, and inflammation. Mice in this experiment had to be euthanized by 12–13 months of age because they developed skin cancers by that age. We examined mice in 2 age groups, 1 at ages 6–7 months and the end point age of 12–13 months (Figure 3). In this second phase of our study, we hoped to increase hyperplasia and dysplasia using 3 tamoxifen injections at 6–8 weeks of age and then 1 dose every 2 months; however, hyperplasia-metaplasia, inflammation, and dysplasia alterations were similar to those observed in the first phase of experiments described previously for p16KO versus p16WT mice.

There were significant differences in grades of dysplasia among the different models ($P = 4e-06$ overall, $P = .00016$ at 6–7 months, and $P = .041$ at 12–13 months; Figure 3*A-C*). Mice carrying both p16KO+Kras12D had the highest frequency of higher-grade dysplasia (post-hoc pairwise adjusted P-values of p16KO+Kras12D compared to: p16WT+KrasWT, or p16KO, or Kras12D were $P = .0036$ overall, $P = .017$ at 6-7M, and $P = .16$ at 12-13M). Kras12D mice had significantly more dysplasia than control animals at age 6–7 months ($P = .017$) but did not reach statistical significance at age 12–13 months. Overall, only mice carrying both p16KO+Kras12D had grade 3 dysplasia (82%, $P = .0004$), and only p16WT+KrasWT mice had no dysplasia (33%). These data support the notion that $KRAS^{G12D}$ synergizes with CDKN2A-p16 loss of expression in LGR5-derived cells enhancing glandular dysplasia.

The analysis showed increased mucous gland hyperplasia/metaplasia scores compared with control p16WT/KrasWT mice in p16KO+KrasWT ($P = 4.02e-03$), Kras12D ($P = 4.02e-03$), and albeit there was increased hyperplasia/metaplasia in p16KO+Kras12D mice it did not reach significance ($P = .11$). There were no significant differences in glandular hyperplasia-metaplasia scores between p16KO, Kras12D, and p16KO+Kras12D mice (Figure 3*D-F*).

Deletion of p16 was also associated with increased SCJ inflammation scores in p16KO (50% were 3+) and p16KO+Kras12D (27% were 3+) as compared with p16WT and KrasWT mice where 0% had 3+ inflammation scores, but there was no statistical significance among the various models ($P = .18$).

To demonstrate that $KRAS^{G12D}$ was expressed in the nodular areas of hyperplasia and dysplasia we attempted immunohistochemistry; however, the available commercial antibody was not able to specifically detect $KRAS^{G12D}$ protein. We therefore tested the expression of phospho-ERK (pERK) phospho-p42 and p44, respectively phosphorylated at residues T^{202}/Y^{204} and T^{185}/Y^{187} by MEK1 and MEK2 kinases downstream of Ras, by immunohistochemistry and could detect increased pERK protein in SCJ glandular tissues of mice carrying Kras12D genotype versus control (Figure 1*R* and *S*). Furthermore, in subsequent experiments where we performed RNA sequencing (RNASeq) transcriptomic analysis of 3D organoids isolated from the SCJ segment of the stomach of mice carrying Kras12D genotype and treated with tamoxifen, we detected 8%–13% of *Kras* transcripts with the G12D mutation, confirming expression of oncogenic *Kras*.

There were no statistically significant differences between males and females in gland hyperplasia/metaplasia ($P = .12$; BF10 = 0.75) and dysplasia ($P = .4$; BF10 = 0.44) for all models, consistent with previous data on the p16WT mice.[6] The Bayes' factor BF10 was less than 1 for all comparisons, which provides evidence for the null hypothesis that there are no significant differences between males and females. Similarly, Bayesian analysis showed substantial evidence in favor of the null hypothesis that there were no significant differences between age groups (BF10 = 0.1 for the single-injection 4-, 9-, and 15-month age groups and BF10 = 0.005 for the multiple-injection 6–7 and 12–13 month groups).

Figure 1. (***See previous page***). **Gross lesions and histologic alterations in mice squamocolumnar junction and stomach.** (*A*) p16WT/KrasWT, (*B*) p16KO/KrasWT, (*C*) p16WT/Kras12D, and (*D*) p16KO/Kras12D. Progressively increasing thickening of SCJ is seen from p16WT/KrasWT to p16KO/Kras12D. Scales are in millimeter. Hematoxylin and eosin–stained SCJ sections at 200x original magnification. p16WT/KrasWT mice show small numbers of cardia-type mucous glands (*E*), whereas larger numbers of mucous glands indicate increased mucous gland hyperplasia/metaplasia in p16KO/KrasWT mice (*F*). Low-to-moderate-grade dysplasia (grade 1-2) was the maximum dysplastic phenotype of SCJ glandular epithelium in most p16WT, p16KO, and Kras12D mice (*G*), whereas high-grade dysplasia (grade 3) was seen in Kras12D+p16KO mice (*H* and *I*). Sections of the SCJ of p16KO mice imaged for ROSA26-tdRFP (*J*), LGR5-IRIS-GFP (*K*), and merged tdRFP and GFP (*L*). (*M, N*) Immunohistochemistry for p16 in p16WT and p16KO SCJ glandular epithelium. (*O, P*) Quantitative multiplex immunofluorescence imaging of Ki67 in p16WT and p16KO SCJ glandular epithelium visualized in "Pathology View" mode simulating immunohistochemistry staining. (*Q*) Increased Ki67 proliferation rates in p16KO mice SCJ glandular tissue as assessed by quantitative multiplex immunofluorescence digital image analysis with Inform (Akoya). (*R, S*) Immunohistochemistry for pERK in p16WT and p16KO SCJ.

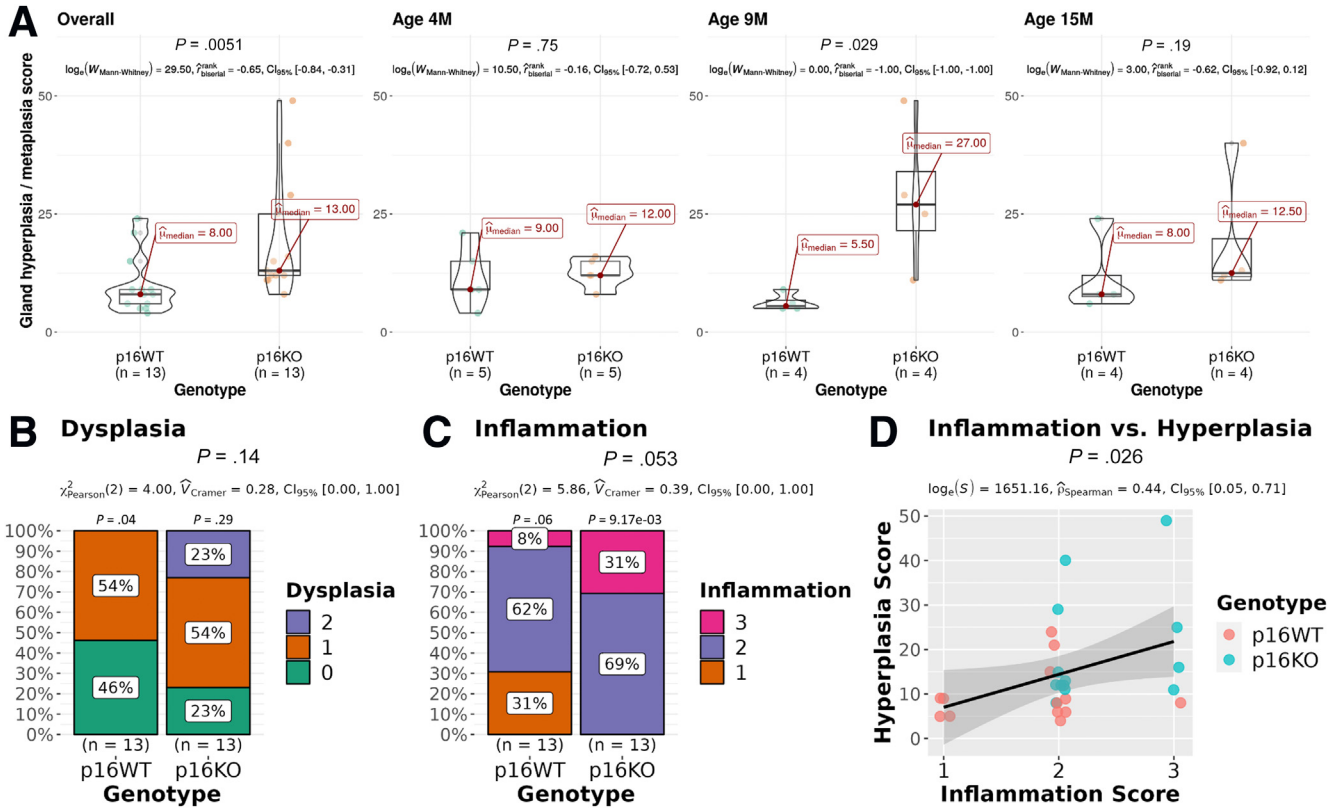

Figure 2. SCJ mucous gland hyperplasia and metaplasia in p16 deleted (p16KO) versus nondeleted mice (p16WT) mice. Histologic sections from the SCJ of p16WT mice and p16KO mice ages 4, 9, and 15 months were examined, and the hyperplasia/metaplasia score was calculated based on the number of mucous glands in the SCJ. (*A*) The data show overall significantly increased mucous gland hyperplasia/metaplasia associated with deletion of p16 in the SCJ ($P = .0051$), which was also statistically significant in mice in the 9-month-old group ($P = .029$). (*B*) Dysplasia scores in p16KO versus p16WT mice, scored for dysplastic features with a scale of 0–3, showed more frequent and higher grades of dysplasia in the p16KO mice but this did not reach statistical significance ($P = .14$). (*C*) Inflammation was scored with a scale of 0–3 in p16KO and p16WT mice. No mice showed absence of inflammation. p16KO mice had higher inflammation scores but this did not reach statistical significance ($P = .053$). (*D*) Significant Spearman correlation between the inflammation score and the mucous gland hyperplasia/metaplasia scores ($P = .026$).

No significant alterations were seen in the stomach, small intestine, or colon of 18 p16KO and 7 p16WT mice. Alterations of antral stomach and intestine in $KRAS^{G12D}$ mice are being reported elsewhere.

In Vivo *Bioluminescence Measurement of p16 Expression in the Stomach Area of Mice With p16 Deletion in LGR5$^+$ Cells*

The luciferase signal in p16Luc mice reflects p16 expression, which can increase in proliferative, hyperplastic cells and therefore serve as a surrogate marker of the size and growth of SCJ lesions.[18] We crossed p16FF with p16Luc mice to generate conditional *Lgr5*-Cre-mediated homozygous p16 knockout (p16FLuc) mice. P16FLuc mice express firefly luciferase instead of p16 under the control of the p16 promoter in 1 allele and on tamoxifen treatment delete the endogenous p16 exon 1 in LGR5$^+$ cells in the other allele, resulting in loss of p16 expression, similar to p16KO mice. In addition, we crossed p16FLuc mice with Kras12D mice to measure the *in vivo* effects of combined p16 deletion and $KRAS^{G12D}$ activation in the SCJ LGR5$^+$-derived lineages. All mice were given BA in drinking water to resemble human reflux disease as described in Materials and Methods. The mice were imaged from the age of 4 months once every other month until 15 months of age. Localized expression of luciferase was confirmed by immunofluorescence and real-time polymerase chain reaction of RNA extracted from the SCJ, stomach, small intestine, and colon (not shown).

P16FLuc mice treated with tamoxifen and BA (resulting in p16KO and loss of p16) compared with control BA treatment alone (expressing p16 from 1 allele) showed significantly increased luciferase expression driven by the p16 promoter (Figure 4). In addition, like p16KO+Kras12D mice, p16FLuc+Kras12D mice showed a synergistic increase in p16-driven luciferase expression in the stomach area consistent with increased size of SCJ lesions. The average amount of p16 promoter-driven luciferase expression increased with age, particularly in tamoxifen-treated p16FLuc and p16Fluc+Kras12D mice. These results are consistent with the observed synergistic effect of p16 deletion and KRAS activation in driving SCJ gland dysplasia.

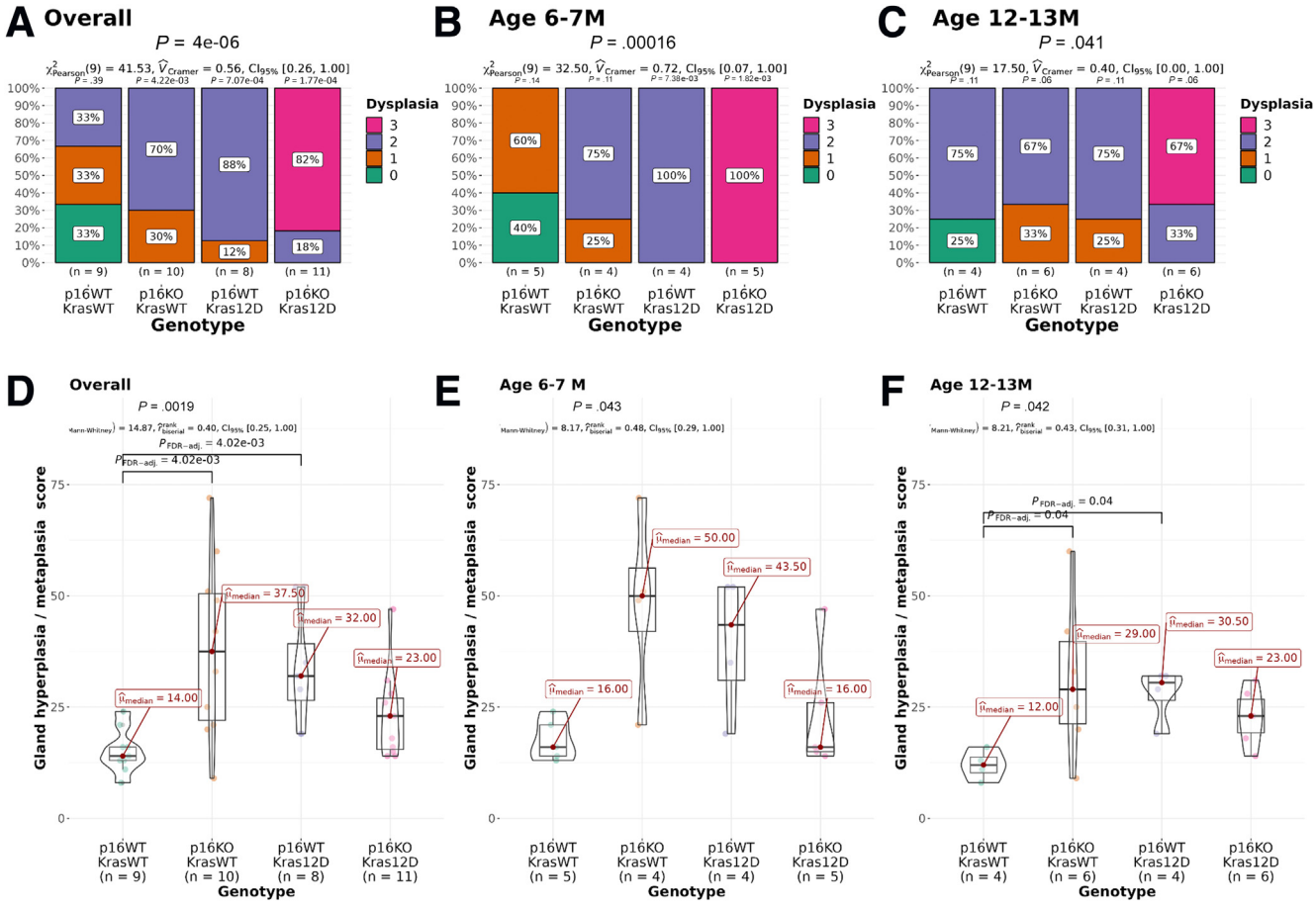

Figure 3. Effect of p16 deletion (p16KO), KRAS activation (Kras12D), and the combination of p16 deletion and Kras activation (Kras12D/p16KO) compared with control mice (p16WT/KrasWT) in SCJ glandular dysplasia scores (*A-C*) and SCJ mucous gland hyperplasia/metaplasia scores (*D-F*), in mice of 2 age groups: 6–7 months or 12–13 months.

Transcriptome Analysis of SCJ Lesions and Derived Organoids

We first performed transcriptome microarray and RNASeq analysis of SCJ from both p16WT and p16KO mice. Separate areas of SCJ glandular or squamous tissue were used after microdissection for microarray assays. Comparison of squamous versus SCJ glandular expression in both p16WT and p16KO mice showed upregulation of genes associated with gastric and intestinal glandular cell differentiation (eg, *Muc1*, *Muc6*, *Krt7/8/18/19/20*, *Tff2*) and downregulation of genes associated with squamous epithelium (eg, *Krt1/4/5/6a/6b/10/13*, *Dsg1b/1c*, *Dsc1*) (Supplementary Table 1).

Differential expression analysis (Supplementary Tables 2 and 3) showed substantial overlap in microdissected glandular tissues with differentially expressed genes and pathways reported by Quante et al[6] in the SCJ of IL1b mouse model and in human BE as compared with the corresponding squamous epithelium including *Krt18*, *Cldn18*, and *Muc5AC*, supporting that it models human Barrett's metaplasia. Our microarray data showed evidence of gastric metaplasia (high expression of *Tff1*, *Tff2*, *Muc6*, *Muc5ac*, *Gkn3*) and evidence of limited intestinal differentiation, including expression of *Itln1*, *Muc4*, *Muc5b*, *Muc13*, *Spink4*, and low level *Tff3*, but showed no evidence of expression of goblet cell markers *Cdx1*, *Cdx2*, Guca2a, or *Muc2* in either p16KO or p16WT mice SCJ.

Similarly, differentially expressed pathways that characterize the glandular metaplastic process in the SCJ of IL1b mice, p16WT, and p16KO mice include MAP kinase, WNT, cholesterol metabolism, and oxidative stress pathways (Supplementary Table 3).

Differential transcriptome analysis of microdissected SCJ glands (Supplementary Table 4) showed several pathways enriched in differentially expressed genes in p16KO SCJ as compared with p16WT mice using either TAC software (Supplementary Table 5) or subnetwork pathway enrichment with the *pathfindR* package (Supplementary Table 6). The top WikiPathway 20 clusters enriched in p16KO versus p16WT SCJ are shown in Figure 5 and the differentially expressed gene network for the top 20 WikiPathways enriched in p16KO SCJ are illustrated in Figure 6. Significantly enriched pathways in p16KO SCJ include apoptosis (subnetwork enrichment P = 1.6e-5), proteasome degradation (P = 5.8e-11), DNA damage response via ATM (P = 1.8e-9), tumor necrosis factor-α signaling (P = 5.2e-6), p53

network (P = .002), EGF/EGFR signaling (P = 3.3e-12), ErbB signaling pathway (P = 3.2e-7, clustered with mitogen activated protein kinases (MAPK) cascade (P = 5.4e-6), RAS signaling (P = 7.1e-9), and G1 to S control (P = 6.1e-11; clustered with cell cycle pathway, P = 6.6e-11). The genes altered in the cell cycle pathway include known targets of p16 controlling the G1 to S transition that were upregulated in microdissected SCJ glands with p16 deletion (*Cdk4*, *Cdk6*, *Ccnd2*, and *Ccne1*), whereas genes associated with G2 and M, such as *Cenpf*, *Aurka*, and *Bub1*, were not upregulated by p16 deletion.

RNASeq of whole SCJ of p16WT and p16KO mice was also performed (Supplementary Table 7). Comparison of overlapping RNASeq differentially expressed genes with the microarray analysis (Supplementary Table 8) shows upregulation in p16KO of cyclin D2, antiapoptosis/nuclear factor-κB target *Bcl3*, and various genes enriched in gastric mucosal cells, including *Vnn3*, *Slc35c1*, and *Tmc7*; and downregulation of several genes including WNT receptor *Fzd2*, immune regulator *Cd200*, ketogenesis enzyme *Hmgcs2,* proapoptosis regulators *Cyfip2* and *Casp4*, chaperone *Cryab*, and desmin-associated protein *Synm*. Note that the SCJ samples for RNASeq included columnar epithelium, mucous glands, squamous epithelium, stroma, and muscularis components of the stomach wall and therefore it is difficult to distinguish gene expression changes in the glandular versus other tissues, whereas microarray samples examined highly enriched microdissected SCJ mucous glands and columnar epithelium.

To establish *in vitro* culture models of BE precursor cells and tissues with well-defined genetic backgrounds we isolated organoids from the SCJ of p16KO and p16WT mice (Figure 7*A*). Single-cell RNA sequencing (scRNASeq) was performed on isolated organoids and UMAP density plots of normalized data showed similar clusters in p16KO and p16WT mice (Figure 7*B*). p16KO and p16WT organoids expressed glandular cell markers, such as *Krt7*, *Krt19*, *Krt20*, and *Muc1*, and gastrointestinal progenitor cell markers, such as *Lgr5* in rare cells (Figure 7*E*), and *Msi*, *CD44*, *Bmi1*, *Prom1*, and *CD44*, but showed no evidence of terminal gastric or intestinal differentiation (Supplementary Table 9). *Cdkn2a* expression, which includes p16 and p19 transcripts, was distributed throughout the organoids, with highest expression in clusters 1, 4, and 8 in p16WT; furthermore, *Cdkn2a* expression was reduced in clusters 1, 4, and 8 in p16KO compared with p16WT organoids (Figure 7*C* and *D*). In addition, transcript analysis of *Cdkn2a* gene expression with the integrated genome viewer showed a reduction of the average ratio of p16 exon 1a to p19 exon 1b in p16KO (21%) compared with p16WT (44%), supporting the conclusion that there was effective deletion of p16 in the SCJ from which p16KO organoids were derived.

Clusters 4 and 8 represent cells with the highest expression of *Cdkn2a*, progenitor cell marker *Lgr5*, and glandular differentiation markers, including *Krt19*/*20* and *Muc1*. Genes differentially expressed between p16KO and p16WT in clusters 4 and 8 included *S100a4*, *Adamts5*, *Renbp*, *Plet1*, *Pros1*, *Hey1*, *Hoxa1*, *Hoxa4*, *Il13ra2*, *Rbp1*, and *Slc16a3* (Figure 7*E* and Supplementary Table 10).

Pathway analysis of p16KO SCJ organoids compared with p16WT with *pathfindR* showed various altered pathways also identified by microarray analysis in the SCJ glands in vivo, including EGF/EGFR (P = .0002), RAS (P = .006), and MAPK (P = .006) signaling, cell cycle (P = .003), G1 to S control (P = .006), ATM signaling (P = .004), Rb in cancer (P = 6.8e-6), apoptosis (P = .03), tumor necrosis factor-α signaling (P = .008), and Parkin-ubiquitin proteasomal system (P = .001) pathways (Supplementary Table 11). Additional pathways differentially altered in p16KO versus p16WT organoids included cell differentiation (P = .0003), ectoderm differentiation (P = .01), preimplantation embryo (P = 9.5e-5), Hippo signaling regulation (P = .0002), transforming growth factor-β receptor signaling (P = 1.7e-4), transforming growth factor-β signaling for epithelial-mesenchymal transition (P = 2.7e-5), and epithelial-mesenchymal transition in colorectal cancer (P = .004) pathways.

The transcriptomic data in mouse SCJ glands and organoids, combined with the observed enhanced SCJ gland hyperplasia/metaplasia and alterations in the targets of p16, both in SCJ *in vivo* and SCJ-derived organoids of p16KO mice, represent functional evidence for a role of p16 in SCJ glandular hyperplasia/metaplasia as a stage of Barrett's like metaplasia.

Discussion

Here, we report the effects of conditional LGR5$^+$ cell lineage-specific p16KO and KRAS^{G12D} knock-in on the development of BE-like esophageal glandular hyperplasia/metaplasia and dysplasia in the IL1b mouse model. Earlier work showed that the IL1b mouse model reproduced human BE alterations that were accelerated by exposure to BA and/or nitrosamines, progressing to dysplasia and adenocarcinoma,[6] and that BE and EAC may arise from LGR5$^+$ gastric progenitors.[7]

Our data demonstrate that CDKN2A-p16 deletion in LGR5$^+$ cell precursors is associated primarily with increased mucous gland hyperplasia/metaplasia. SCJ histology of p16KO mice exhibited larger areas of hyperplastic/metaplastic mucous glands compared with p16WT mice, with higher numbers of mucous glands showing more complex glandular architecture, supporting a role for p16 in the early development of Barrett's metaplasia. These data are consistent with our findings in human Barrett's, where we found an increased prevalence of *CDKN2A* genomic alterations in 69% of patients with nondysplastic BE 1 or more years before they progressed to esophageal dysplasia, compared with 21% of patients with BE that did not progress to dysplasia or EAC.[3]

In human EAC, RAS amplification or activating mutations are present in 18%–40% of cases.[20,21] We tested whether KRAS^{G12D} activation alone or in combination with p16 deletion would affect SCJ gland hyperplasia/metaplasia and dysplasia in the mouse model. We found that oncogenic KRAS activation alone could drive SCJ gland hyperplasia/metaplasia and dysplasia in IL1b mice with bile acid injury. KRAS^{G12D} expression resulted in significantly increased SCJ glandular dysplasia scores as compared with p16WT mice

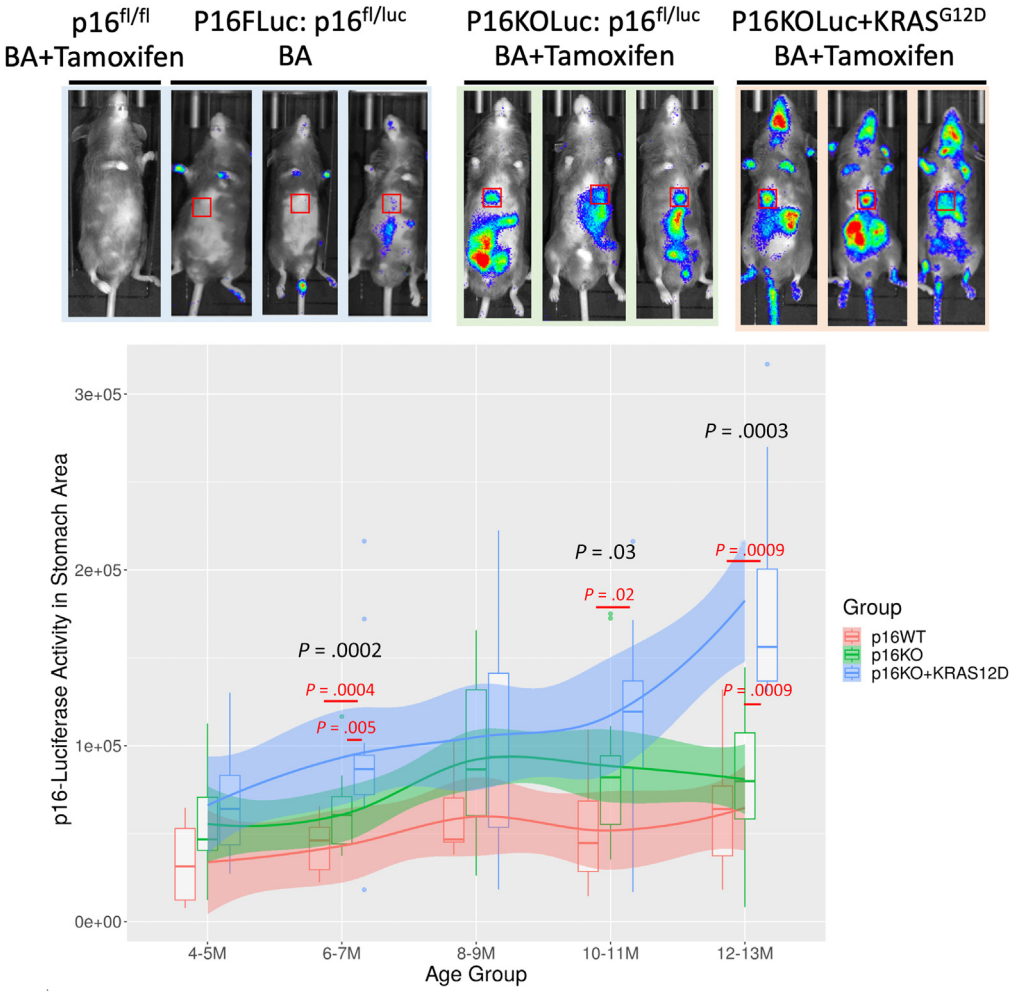

Figure 4. In vivo detection of bioluminescence with IVIS instrument, reflecting expression of luciferase driven by the CDKN2A-p16 promoter in mice with homozygous floxed p16 ($p16^{fl/fl}$), mice with 1 floxed p16 allele and 1 p16 allele replaced with luciferase ($p16^{fl/luc}$), or mice with 1 LoxP-Stop-LoxP-KrasG12D allele ($Kras^{G12D}$). All mice were treated with BA to simulate bile reflux. After treatment with tamoxifen, p16 is deleted and $Kras^{G12D}$ is expressed in Lgr5-positive cells expressing Lgr5-Cre. Mice without p16-luciferase ($P16^{fl/fl}$) and mice treated only with BA (P16FLuc) were used as control animals. (*Bottom*) Boxplots of quantitative measurements of luciferase luminescence in the stomach area (*red square*) from $p16^{fl/luc}$ treated with BA alone (p16FLuc) as compared with $p16^{fl/luc}$ (P16KOLuc) and $p16^{fl/luc}Kras^{G12D}$ (p16KOLuc+$KRAS^{G12D}$) treated with BA plus tamoxifen. *Shaded areas* surrounding each line represent 95% confidence intervals. For each age group, the *P values in black* represent significant differences among the 3 groups (nonparametric 1-way ANOVA) and the *P values in red* represent statistically significant pairwise differences between the 2 groups indicated by the *red lines* (FDR-adjusted Dunn test).

and mice carrying the combination of KRAS activation and p16 deletion showed the highest frequency and grades of dysplasia, with 82% of p16KO+Kras12D mice developing grade 3 (high-grade) dysplasia. Furthermore, high-grade dysplasia developed earlier and could be observed in the SCJ of p16KO+Kras12D mice by 6 months of age, but not in either single-alteration model alone. P16 loss and $KRAS^{G12D}$ were not sufficient to induce the development of invasive adenocarcinomas in the mouse models. The data indicate that KRAS activation and P16 deletion are synergistic in the development of SCJ glandular dysplasia and accelerate the development of lesions seen in the early stages of esophageal carcinogenesis and suggest that additional alterations are required for invasive cancer development.

To further our understanding of the molecular mechanisms underlying the hyperplasia and dysplasia in mouse SCJ glandular tissues and in derived 3D organoids we performed transcriptome analyses. Among the most significant transcriptome alterations we found that CDKN2A-p16 deletion is associated with increased G1 to S transition, and decreased apoptosis and senescence mRNA expression signatures. This is consistent with the known roles of CDKN2A as a negative regulator of the cell cycle, particularly: transition from G0 to G1, through inhibition of Rb-phosphorylation by CDK4/CDK6/CyclinD1/D2 complexes; and transition from G1 to S transition, by inhibiting the CDK2/CyclinE complex.[9,22] In addition to these post-transcriptional roles of p16, our transcriptome analyses

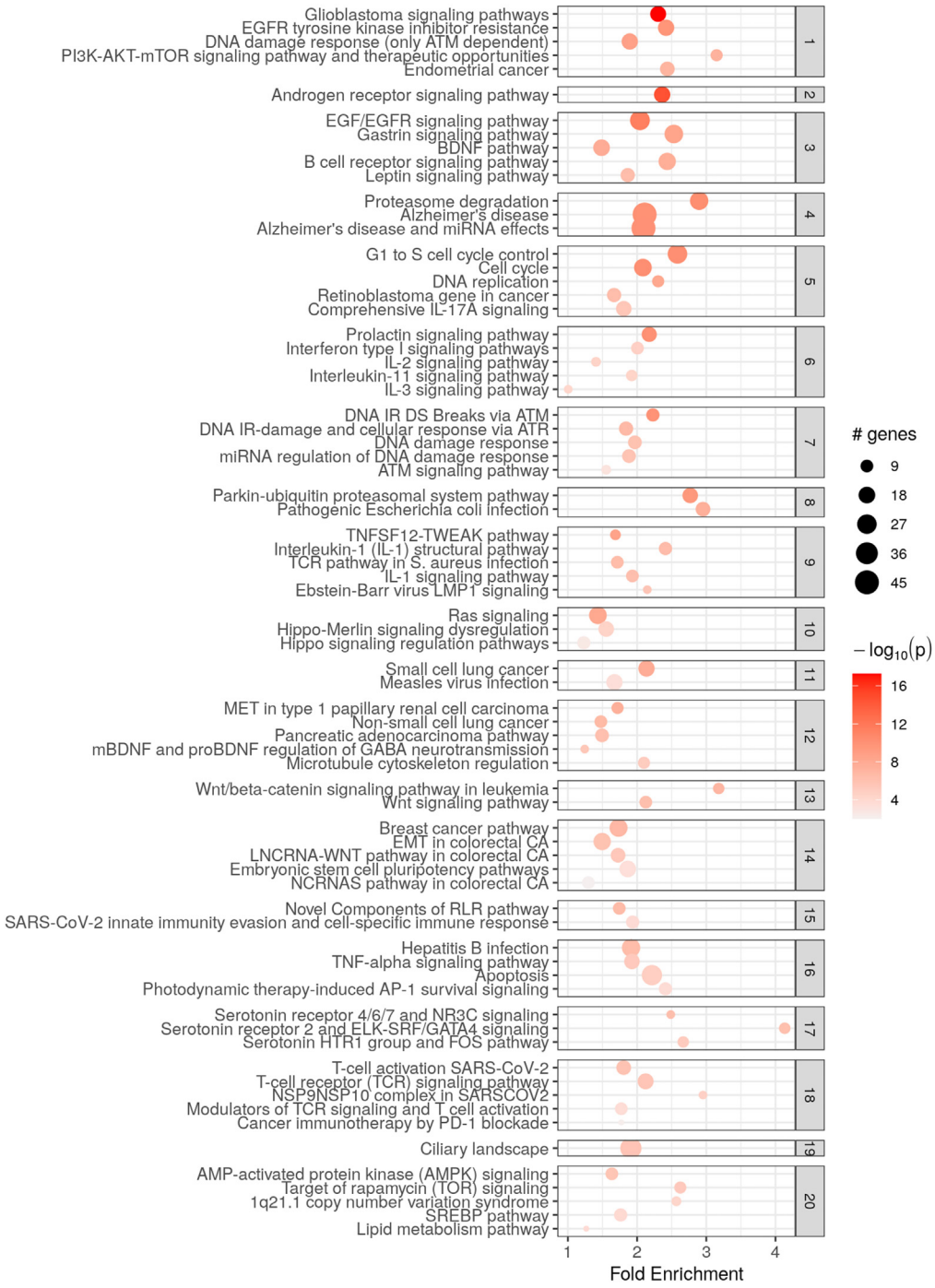

Figure 5. Pathway analysis of p16KO versus p16WT SCJ glandular lesional tissue after laser capture microdissection and microarray expression analyses. WikiPathways were analyzed with the R package *pathfindR*,[19] ranked based on subnetworks of protein-protein interactions of the differentially expressed genes and grouped into clusters using hierarchical clustering of differentially expressed genes common to multiple pathways. The top 20 clusters (in the *gray labels on the right*), and up to the top 5 pathways (*labelled on the left*) for each cluster are shown. Each pathway is represented by a *circle*, positioned in the x-axis according to the relative pathway activity in p16KO versus p16WT mice. The size of the *circle* represents the number of differentially expressed genes in the pathway and the intensity of the *red color* is inversely proportional to the *P* value for the pathway enrichment in p16KO versus p16WT mice.

showed that *cyclin D2*, *cyclin E*, *Cdk4*, and *Cdk6* transcripts were increased by p16 deletion, possibly as a consequence of increased numbers of cells in the G1 and S phases.

In normal cells, on mitotic stimulation, predominantly through receptor tyrosine kinases, Ras, and MAPK, failure of cells to progress to S and G2 phases triggers senescence checkpoints involving p16→Rb and CDKN2A/p19→TP53→CDKN1A/p21.[23] Our p16Luc mice data further suggests that $KRAS^{G12D}$ induces p16 promoter activity in SCJ lesions, consistent with the known role of oncogenic KRAS in activating p16 and oncogene-induced senescence.[24] In our transcriptome analyses of mouse SCJ lesions, p16 deletion resulted in decreased activity of senescence and apoptosis pathways, consistent with the known role of p16 in these pathways and suggests that bypass of oncogene-induced senescence and apoptosis in the absence of p16 may be a mechanism for our observed synergy of p16 deletion and KRAS activation in promoting

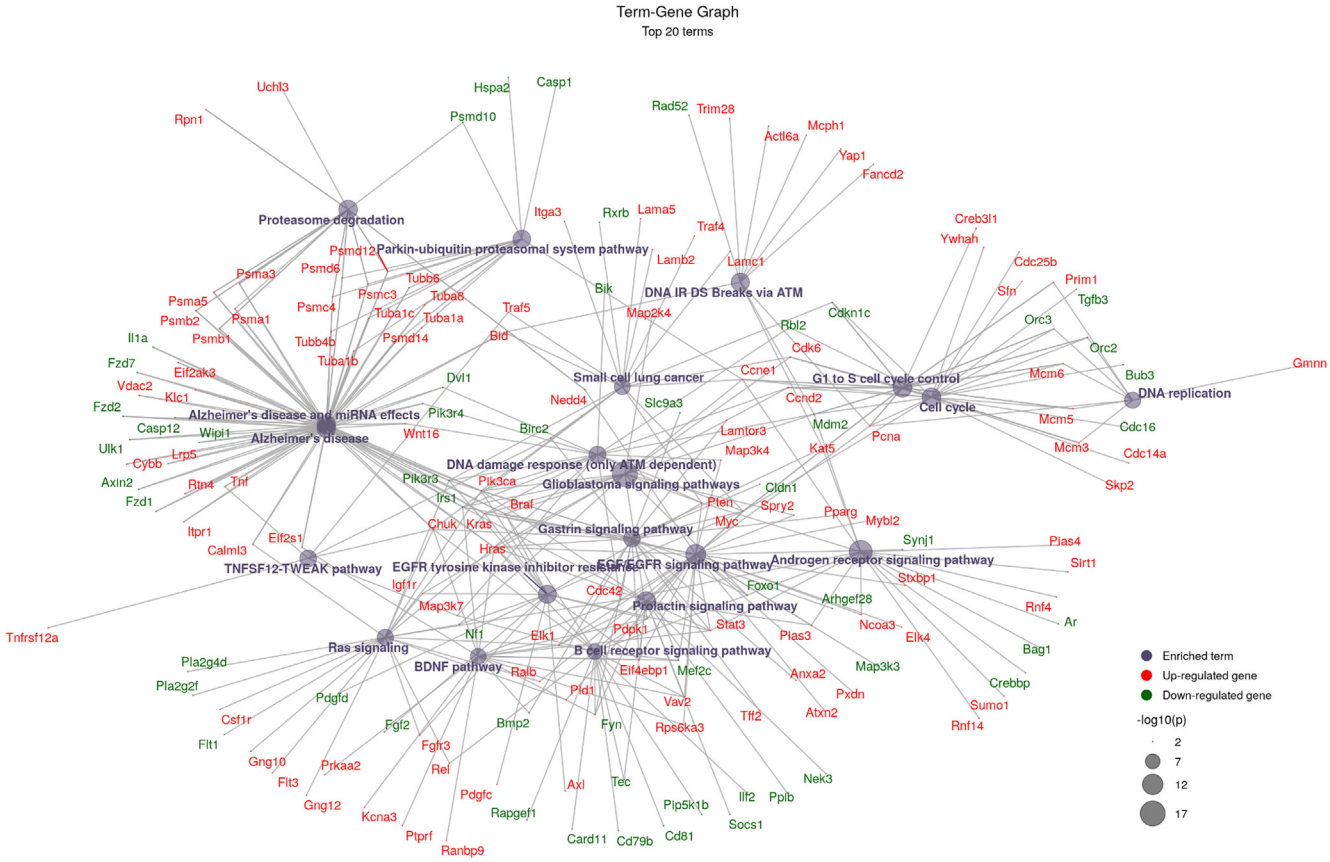

Figure 6. Network graph of the top 20 WikiPathways differentially enriched in the SCJ of p16KO versus p16WT mice. In this graph, each *dark blue node* represents a WikiPathway, and the size of the WikiPathway node is inversely proportional to the *P* value. The differentially expressed genes are connected to each pathway by a *line* and are labelled in *red* if increased in p16KO versus p16WT SCJ, and in *green* if decreased in p16KO versus p16WT SCJ.

SCJ dysplasia. Furthermore, as p16KO resulted in activation of MAPK and RAS pathways, this might have provided an increment of these pathways as they are constitutively activated by $KRAS^{G12D}$, underlying the synergistic effect of p16 deletion and oncogenic KRAS on dysplasia progression.

Future studies of transcriptome alterations in the SCJ and derived organoids of the activated KRAS mouse models may provide further details of the interplay between p16 and KRAS pathways in adaptive cellular responses that result in uncontrolled cellular proliferation and dysplasia.

In summary, the mouse models described here, combining inflammatory injury through IL1b pathway activation, bile acid injury, deletion of p16, and activation of KRAS, accelerated Barrett's-like glandular hyperplasia/metaplasia and dysplasia in the squamocolumnar region of mice, reproducing human Barrett's progression to high-grade dysplasia. These *in vivo* models may be useful for preclinical studies targeting KRAS activation and p16-regulated CDK4/6, which may be explored as potential therapeutic interception approaches to prevent esophageal adenocarcinoma development in humans, and to further study the functional outcomes of complex genomic alterations that replicate the multiple genomic landscapes of esophageal precancer.

Materials and Methods

All authors had access to the study data and reviewed and approved the final manuscript.

Mouse Models

We have established 6 mouse models carrying targeted genetic alterations to study the role of CDKN2A-p16 and activated $Kras^{G12D}$ in epithelial glandular cells derived from LGR5 progenitor cells in mouse SCJ. The genotypes of our 6 established mouse models are as follows: p16WT: *Lgr5-Cre*$^{+/-}$, *IL1B*^{tg}; *p16*$^{w/wt}$; p16FF: *Lgr5-Cre*$^{+/-}$, *IL1B*^{tg}; *p16*$^{flox/flox}$; p16FLuc: *Lgr5-Cre*$^{+/-}$, *IL1B*^{tg}; *p16*$^{flox/luc}$, Kras12D: *Lgr5-Cre*$^{+/-}$, *IL1B*^{tg}; *p16*^{wtwt}; *Kras*$^{LSL-G12D}$, p16FF+Kras12D: *Lgr5-Cre*$^{+/-}$, *IL1B*^{tg}; *p16*$^{flox/flox}$; *Kras*$^{LSL-G12D}$ and p16FLuc+Kras12D: *Lgr5-Cre*$^{+/-}$, *IL1B*^{tg}; *p16*$^{flox/luc}$; *Kras*$^{LSL-G12D}$. In addition to these genetic alterations, some mice also carried a tomato red fluorescent protein (tdRFP) reporter gene (*ROSA26-flox-STOP-flox-tdRFP*), as a marker of Cre-mediated recombination.[25]

To establish our mouse models we bred mice with the following genotypes: *Lgr5-Cre*$^{+/-}$ (*Lgr5-EGFP-IRES-creERT2*), *IL1B*^{tg} (*Tg*[*ED-L2-IL1RN/IL1B*]), *p16*$^{flox/flox}$ (*CDKN2A-LOX-Exon1A-LOX*), *p16*^{luc} (*CDKN2A-LUC-SV40pA*,

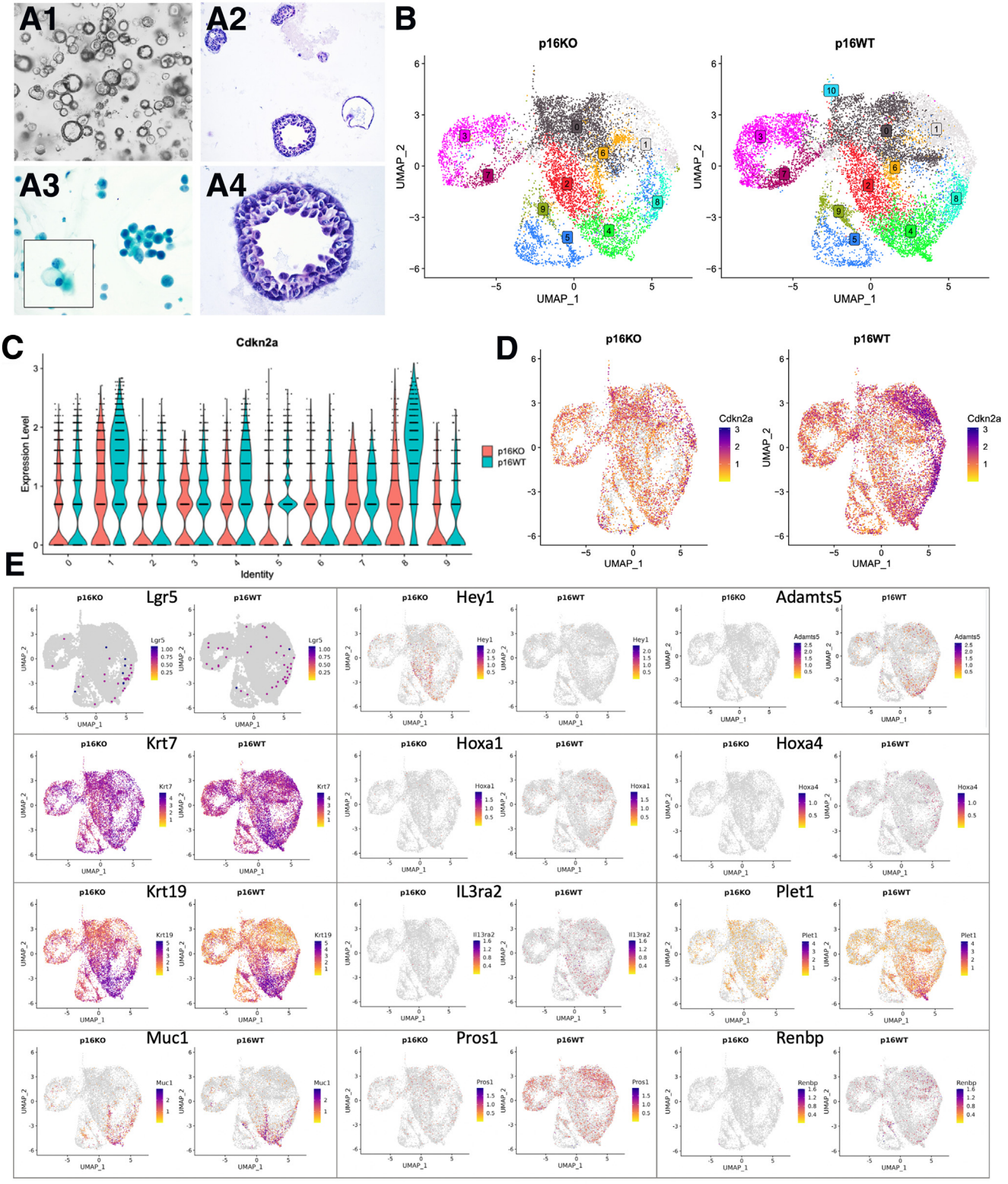

Figure 7. Histology and scRNA analysis of SCJ organoids derived from p16WT and p16KO mice. (*A*) Organoid histology: 3D culture of organoids derived from the SCJ of p16KO mice. A1: 3D culture in Matrigel visualized by phase contrast microscopy. A2, A4: Hematoxylin and eosin stain of cell block preparations. A3: Alcian blue stain of a cellular smear prepared from p16KO organoids. (*B-D*) Organoid scRNASeq. (*B*) UMAP dimensional plots of cell clusters from p16WT and p16KO organoids. (*C*) Violin plot of *Cdkn2a* expression in UMAP clusters 0–9, showing reduced Cdkn2a transcripts in clusters 1, 4, and 8 in p16KO (*red*) compared with p16WT (*blue*) organoids. (*D*) UMAP visualization of Cdkn2a-expressing cells colored by level of *Cdkn2a* expression, in p16KO (*left*) and p16WT (*right*) organoids. (*E*) Gene expression UMAP in clusters 4 and 8, which are characterized by higher number of *Lgr5*$^{+}$ cells (*E, top left*), partial glandular differentiation (*Krt19* and *Muc1* expression, *E, left column*), highest *Cdkn2a* expression (*D*), and highest difference in *Cdkn2a* expression between p16KO and p16WT (*C*). *Middle* and *right columns* in *E* show UMAPs of cells expressing genes showing significant differential expression in both cluster 4 and cluster 8 between p16KO and p16WT organoids.

inserted into *Cdkn2a* Exon 1a), and *LSL-Kras^{G12D}* (*LoxP-STOP-LoxP- Kras^{G12D}* inserted into the endogenous *Kras* gene; *Kras^{G12D}* expression requires Cre-mediated recombination). The original breeder mouse lines were *Lgr5-EGFP-IRES-creERT2*,[26] *IL1B^{tg}*,[6] and *LSL-Kras^{G12D}*,[27] kindly given by the laboratory of Dr Timothy Wang; *p16^{luc}*,[18] kindly given by Dr Ned Sharpless laboratory, and *p16$^{flox/flox}$*,[17] kindly given by Dr Gloria Su's laboratory.

To inactivate p16, we used a p16 conditional knockout model[17] with exon1a of *Cdkn2a* flanked by loxP sites. On treatment with tamoxifen at age 6–8 weeks Cre-mediated recombination occurs in LGR5^{+} cells, creating tissue-specific p16 knockout mice.[26] Mouse studies were approved by the George Washington University IACUC protocol committee. All mice were fed standard irradiated feed (LabDiet 5V75) and bedded in corn cob bedding (1/8" Bed-O-Cob) in individually ventilated cages (Tecniplast emerald line). Interventions were done during the light cycle.

Treatment of Mice With Tamoxifen and Bile Acid

Mice were treated with tamoxifen to induce Cre-mediated recombination resulting in tissue-specific p16 deletion and/or KRAS^{G12D} expression. At the age of 6–8 weeks, 133 mg/kg of tamoxifen (Sigma-Aldrich, St Louis, MO) was administered to mice via intraperitoneal injection every 48 hours, for a total of 3 injections to induce Cre-activity in Lgr5^{+} cells. Thereafter, tamoxifen injections were administered every 2 months. In a subset of mice, we performed only the first set of 3 injections as indicated in the Results section. Starting at the age of 3 months, mice were given 0.2% sodium deoxycholate bile acid (BA) (Sigma-Aldrich) in their drinking water *ad libitum*.[6] Mice were sacrificed from 4–22 months of age to track disease progression. SCJ and stomach tissues were harvested and used to prepare formalin-fixed paraffin embedded and fresh frozen tissue blocks to be used for histologic analysis and other experiments.

Histopathology and Scoring of SCJ Inflammation, Glandular Hyperplasia/Metaplasia, and Dysplasia

Harvested SCJ area tissue was fixed in neutral-buffered 10% formalin, paraffin embedded, and 5-μm sections were stained with hematoxylin and eosin for histopathology. Hematoxylin and eosin sections were evaluated for inflammation, gland hyperplasia/metaplasia, and dysplasia in the SCJ area. Inflammation was scored as grade 1, 2, or 3, based on the presence of inflammatory cells (lymphocytes, plasma cells, and neutrophils) in the squamocolumnar space: grade 1, rare inflammatory cells; grade 2, small clusters of inflammatory cells; and grade 3, large clusters of inflammatory cells. Gland hyperplasia/metaplasia was quantified by counting the numbers of cross-sectional mucous gland profiles at the SCJ; dysplasia grades were 0 (no dysplasia), 1 (focal low-grade), 2 (extensive low-grade), or 3 (high-grade), based on nuclear alterations and architectural complexity of the glandular growth at the SCJ. Pathology scoring was performed by a gastrointestinal pathologist (ARS).

Fluorescence Imaging and Immunohistochemistry of Mouse Squamocolumnar Junction

To detect tdRFP fluorescence, which is a marker of Cre-mediated recombination in mice with the *ROSA26-flox-STOP-flox-tdRFP* genotype, freshly dissected mouse SCJ was fixed in 4% paraformaldehyde–phosphate-buffered saline at 4°C overnight, followed by 30% sucrose overnight. Tissue was then embedded in O.C.T. compound (FSC22 Frozen Section Comp, Leica Biosystems, Muttenz, Switzerland), to create a frozen block. Then, 5-μm sections were cut and mounted with Vectashield with DAPI (Vector Laboratories, Newark, CA). Slides were imaged using a Revolve-Discover fluorescence microscope (Echo Laboratories Inc, San Diego, CA).

To detect p16 in mouse tissues, the p16INK4a mouse monoclonal antibody (1E12E10; Thermo Fisher Scientific) was used at 1:100 dilution, and incubated overnight at 4°C, after blocking the slides at room temperature with blocking reagent (Polyview IHC Kit, Enzo Life Sciences). For visualization, the Bond Polymer Refine Detection Kit (Leica Biosystems) was used, and slides were counterstained with hematoxylin.

To detect pERK, the phospho-p44/42 MAPK (Erk1/2) (137F5) Rabbit mAb (Cell signaling Technology) was used at 1:500 dilution, overnight at 4°C. For visualization, the Bond Polymer Refine Detection Kit (Leica Biosystems) was used, and slides were counterstained with hematoxylin.

To detect KI67 expression in epithelial cells, we performed quantitative multispectral immunofluorescence using the Vectra system (Akoya Biosciences, Marlborough, MA). Briefly, sections of SCJ were stained with a cocktail of primary antibodies including anti-cytokeratin 19 (Abcam ab133496, at 1/200 dilution), to label epithelial cells, and anti-KI67 (Abcam ab15580, at 1/100), to label proliferating cells, followed by several rounds of tyramide signal amplification using horseradish peroxidase-conjugated secondary antibodies, in the OpalTM multiplex 6-plex kits according to the manufacturer's protocol (PerkinElmer-Akoya). Slides were scanned with the Vectra 3.0 Automated Quantitative Pathology Imaging System (PerkinElmer-Akoya Biosciences) and SCJ cells expressing cytokeratin 20 were quantified for the presence of KI67 expression using digital image analysis with inForm Tissue Finder software version 2.4.10 (PerkinElmer-Akoya Biosciences).

In Vivo *Imaging of p16 Promoter Driven Luciferase Activity*

Bioluminescence images were obtained using an IVIS Lumina K instrument (PerkinElmer, Waltham, MA). Mice were anesthetized with isoflurane and abdominal fur was removed by applying hair-removal cream or shaving. Images were taken 10 minutes after intraperitoneal injection (150 mg/kg) of the bioluminescent substrate D-luciferin (PerkinElmer). After injection, mice were transferred to the light-sealed imaging cabinet of the IVIS instrument and

positioned in a nose cone to maintain anesthesia. Bioluminescence images were acquired using a charge-coupled device camera cooled to -80°C to achieve maximum sensitivity. Images were acquired 10 minutes postsubstrate injection with the exposure time of 60 seconds, medium binning, F/stop = 1, and EM gain off. Image data were analyzed with Xenogen Living Image software (PerkinElmer) as described in the Data Analysis and Statistics section.

LCM, RNA Extraction, and Microarray Gene Expression

SCJ tissues were frozen in FSC22 frozen section compound (Leica Biosystems, Richmond, IL). Mucous glands and columnar epithelium in p16WT and p16KO as well as squamous epithelium in p16WT mice samples were microdissected from SCJ tissue sections with LCM using the MicroBeam System (P.A.L.M. Microlaser Technologies GmbH, Germany), equipped with Axiovert 200M microscope (Carl Zeiss Microscopy GmbH, Germany) to harvest at least 1000 cells from the selected SCJ mucous gland areas. The cells of interest were collected in AdhesiveCap 500 opaque tubes (Carl Zeiss) and immediately used for RNA extraction. Total RNA was extracted with the RNeasy plus Micro Kit (QIAGEN, Germantown, MD) following the manufacturer protocol.

Gene expression profiling was performed using the mouse Clariom D Pico assay (Thermo Fisher, Waltham, MA), previously known as GeneChip Mouse Transcriptome Array 1.0 (Affymetrix, Santa Clara, CA) as recommended by the manufacturer. Briefly, 0.3 ng of purified total RNA was used for reverse transcription initiated at the poly-A tail and throughout the entire length of RNA to capture both coding and multiple forms of noncoding RNA. RNA amplification was achieved using low-cycle polymerase chain reaction followed by linear amplification using T7 *in vitro* transcription technology. Then, the cRNA was converted to biotinylated sense-strand DNA hybridization targets for unbiased coverage of the transcriptome. The fragmented and labeled sense-strand DNA was hybridized to the GeneChip mouse WT Array for 16 hours at 45°C and 60 rpm. After hybridization, arrays were washed, stained, and scanned. Data were initially analyzed with Transcriptome Analysis Console 4.0 software (Affymetrix), as described in the Data Analysis and Statistics section.

RNASeq

For RNASeq, total RNA was isolated using RNeasy Plus Micro Kit (QIAGEN). RNA quality was assessed by Agilent 2100 Bioanalyzer and RNA samples with RIN >6.5 were used for sequencing. Briefly, total RNA was used to generate cDNA using Clontech SMART-Seq v4 Ultra Low Input RNA Kit (Takara Bio USA Inc, Mountain View, CA) that uses SMART (Switching Mechanism at 5' End of RNA Template) technology and allows ultra-low RNA inputs. cDNA quality was analyzed using High Sensitivity D5000 ScreenTape (Agilent) and cDNA quantification was performed using Invitrogen Qubit dsDNA HS Assay (Invitrogen, Waltham, MD). To create the library, we used 150 ng of the cDNA and performed DNA fragmentation, tagging with sequencing adapters, followed by library amplification, clean up, and normalization using Nextera XT DNA Library Prep Kit (Illumina Inc, San Diego, CA),) and following the kit protocol.

SCJ 3D Organoid Cultures

The mouse SCJ organoid cultures were established based on the procedure described previously.[28] The stomachs from p16WT and p16KO mice were opened along the greater curvature, washed, and placed flat on a hard surface and the area of SCJ (~1 cm length and 1.5–2 mm width) along the line between the forestomach and cardia/transition to stomach oxyntic segment was dissected for culture in Matrigel (Corning, Corning, NY). Cell pellets were resuspended in Matrigel (Corning), seeded onto a preheated 24-well plate (~10^5–2 x 10^5 cells in 50 μL Matrigel per well). After 30 minute solidification, 0.5 mL of growth medium (Wnt-conditioned medium supplemented with growth supplements 1:50 B27 [Gibco], 1:100 N2 [Gibco], 50 ng/mL mEGF [Peprotech, Cranbury, NJ], 50 mM *N*-acetylcysteine [Sigma-Aldrich], 5 μg/mL gentamicin [BioWhittaker], 0.5 μg/mL fungizone [Gibco]) was added to each well. Conditioned medium was derived from L-Wnt-3A (CRL-2647, ATTC, Manassas, VA) cell line cultured in advanced DMEM/F12 (Gibco) supplemented with 10 μM HEPES (Gibco), 1:100 Glutamax (Gibco), and penicillin/streptomycin. The organoids were cultured in a humidified incubator at 37°C and 5% CO_2, the growth medium was changed every 2 to 3 days. The organoids were split 1:2 to 1:4 depending on their number and size, every 5 to 10 days.

scRNASeq

For scRNASeq experiments we used Chromium Next GEM Single Cell 3' GEM, Library & Gel Bead Reagent Kit v3.1 (10x Genomics Inc, Pleasanton, CA) following the manufacturer protocol. Organoid cell suspensions in phosphate-buffered saline with 0.04% bovine serum albumin were adjusted to 10^6 cells/mL; about 8 x 10^3 cells were loaded onto Chromium Next GEM Chip G Single Cell and processed in the Chromium Controller instrument for Gel Beads-in-Emulsion generation and followed by barcoding of targeted ~5 x 10^3 cells. Produced barcoded full-length cDNA was purified using silane magnetic beads (Dynabeads MyOne SILANE) and amplified via polymerase chain reaction to generate sufficient mass for library construction as described in the manufacturer protocol. The final libraries comprised standard Illumina paired-end constructs, that contained the P5 and P7 primers used in Illumina bridge amplification and the i7 sample index sequences. The generated libraries were sequenced using the following sequencing configuration: Illumina ~350M PE reads (~105GB) 10X using the Illumina HiSeq 4000 instrument. Data analysis was performed with CellRanger 3.1.0 Software (10x Genomics) and R as detailed next.

Sequencing of Total RNA From Organoids

Cardia/SCJ organoids from p16WTKrasG12D mice were cultured as described previously and RNA extracted with the RNeasy plus Micro Kit (QIAGEN) following the

manufacturer protocol. RNA integrity was tested in Bioanalyzer and only samples with RIN >7 were used for sequencing with Illumina HiSeq and at 2 x 150 bp sequence length, ~350M PE reads (~105GB), and single index per lane. The resulting FASTQ files were aligned to the GRCm39 version of the mouse genome with Star,[29] and visualized with the Integrative Genome Viewer.[30]

Data Analysis and Statistics

Summarized statistical methods are presented in each figure.

Histopathology data analysis. Data were analyzed using the *ggstatsplot* package version 1.0.3.[31] Continuous data, such as the gland metaplasia/hyperplasia score, were binned into age groups and analyzed using the nonparametric Mann-Whitney test for differences among groups and plotted with the *ggbetweenstats* function. Ordinal pathology scores (inflammation and dysplasia) were binned into age groups and analyzed using the Pearson chi-square test and plotted with the *ggbarstats* function. *P* values were adjusted for multiple comparisons using the false discovery rate (FDR) method of Benjamini and Hochberg.[32] Correlation between continuous and ordinal variables was analyzed using Spearman rank correlation and the *ggscatterstats* function. In addition, we performed ordinal logistic regression between inflammation and dysplasia with mouse age at death comparing the different models using the *polr* function from the *MASS* package,[33] using the formulas *polr(Inflammation ~ Genotype + AgeatDeath)* and *polr(Dysplasia ~ Genotype + AgeatDeath)*.

In vivo imaging of p16 promoter driven luciferase activity. Image data were analyzed with Xenogen Living Image software version 4.5.4 (PerkinElmer). A 1 cm^2 square region of interest corresponding to the SCJ area was manually defined in the scan images. Radiance flux counts (photons/second) were averaged over the region of interest and adjusted for time, binning, and radiation losses to define absolute average surface radiance in photons/second/cm^2/steradian. Results were aggregated by model genotype and age at time of measurements, and the results analyzed for each age group with the *grouped_ggbetweenstats* function using nonparametric Kruskal-Wallis 1-way analysis of variance for differences among the 3 groups (p16WT, p16KO, p16WT+p16KO) and pairwise comparisons between 2 groups were further examined using the Dunn test with FDR adjustment for multiple hypothesis testing.

Microarray data analysis. Microarray data was analyzed with Transcriptome Analysis Console 4.0 (TAC) software version 4.0.2.15 (Applied Biosystems/Thermo Fisher). First, data were normalized, summarized, and distributions adjusted for GC content and compression effects using the Signal Space Transformation-Robust Multichip Analysis algorithm.[34] All samples were considered as passed after examination of all QC metrics. For all samples, all hybridization controls performed as expected. Principal component analysis with 3 components showed excellent separation between glandular and squamous samples. Comparisons of differentially expressed genes between groups were performed using the Empirical Bayes (eBayes) analysis of variance method.[35] A probeset (gene or exon) was considered expressed if ≥50% of the samples had "detected above background" scores lower than the detected above background threshold of ≤0.05. Microarray expression differential was further processed using custom R code as described next.

Mouse SCJ RNASeq data analysis. Real-time analysis (RTA, Illumina) was used for base calling and *bcl2fastq2* (version 2.20) for converting BCL files to fastq format, coupled with adaptor trimming. We performed a pseudoalignment to a *kallisto* index created from the mouse GRCm38 transcriptome using *kallisto* (0.44.0).[36] We tested for differentially expressed genes under various conditions using *sleuth*, an R package designed to compute transcript and gene-level differential expression from *kallisto* abundance files.[37] Differential expression was tested for statistical significance using the Wald test, and the *P* values were FDR-adjusted.[32] The direction and magnitude of differential expression was indicted by the beta value, a biased estimate of log2 fold-change. We selected genes significantly decreased with the following criteria: (FDR <0.1 and beta <-0.2) or (unadjusted $P < .05$ and beta <-1). For significantly increased genes, we used (FDR <0.1 and beta >0.2) or (unadjusted $P < .05$ and beta >1). To determine differentially expressed genes overlapping between RNASeq and microarray data, we included all genes that had unadjusted $P < .05$ in both RNASeq and microarray measurements.

scRNASeq data analysis. The sequencing raw data was processed using CellRanger software version 3.1.0 (10X Genomics, Pleasanton, CA) to generate FASTQ files, align reads, and generate feature-barcoded matrices, and preliminary visualization of gene expression was performed using the Loupe Cell Browser (10X Genomics). Subsequent analyses were performed using R. First, the *Seurat* package[38] was used to normalize scRNASeq data. The raw matrix expression data h5 files were read into a Seurat object using the *CreateSeuratObject* function. Data from cells with >18% mitochondrial genes and distinct transcript count <150 were excluded. Cell doublets were excluded using the *scds* package.[39] Integration and normalization was performed using the *SCTransform* approach.[40] Principal component analysis and uniform manifold approximation and projection (UMAP) were performed with *Seurat*. The *clustree* package was used to visualize the optimum number of clusters[41] and the UMAP clusters were visualized with an integrated shared nearest neighbor threshold of 0.3. Differentially expressed genes were identified between all cells of p16KO versus p16WT SCJ organoids using the likelihood ratio test as implemented in the *edgeR* pseudobulk procedure of the *Libra* package (https://github.com/neurorestore/Libra, accessed 12/26/2023), with default settings, using the organoid ID as the *replicate_col* argument to adjust for differences between replicates and minimize false-positive results.[42] We also compared each UMAP cluster (0–9) between p16KO and p16WT SCJ organoids to look for cluster-specific differential gene expression, using the *Libra edgeR* procedure and the cluster ID for the *cell_type_col* argument.

Plotting of single-cell expression according to UMAP clusters was performed using the *scCustomize* (https://CRAN.R-project.org/package=scCustomize, accessed 12/27/2023) and *Nebulosa*[43] extensions of the *Seurat* package. Cell cycle scoring was performed with the *CellCycleScoring* function of the Seurat package using the default settings.

Gene set and pathway analysis. For microarray data, pathway analysis was performed using the TAC software and WikiPathways[44] (wikipathways.org) as a source of pathway data. The Fisher exact test was used to compare the frequency of genes passing the filtering criteria in each pathway versus the overall frequency of genes that pass the filtering criteria. Filtering criteria for each gene were differential expression $P \leq .05$, absolute fold-change ≥ 1.5, and average log2 expression ≥ 4. Pathways with Fisher exact test $P \leq .05$ were considered differentially altered between conditions.

We further analyzed the microarray data from laser-captured SCJ of p16KO and p16WT and scRNASeq data from p16KO and p16WT organoids by subnetwork enrichment analysis using the R package *pathfindR*[19] with 692 WikiPathways downloaded from wikipathways.org and from the MiSigDb database.[45] Pathways are ranked by *pathfindR* based on the occurrence of subnetworks determined from known protein-protein interactions of the differentially expressed genes, and then grouped into clusters using hierarchical clustering of differentially expressed genes common to multiple pathways. For this analysis, a gene was considered differentially expressed if the unadjusted $P < .05$, and pathways were discarded from further analysis if the pathway enrichment $P > .05$.

Supplementary Material

Note: To access the supplementary material accompanying this article, go to the full text version at https://doi.org/10.1016/j.jcmgh.2024.01.014.

References

1. Del Portillo A, Lagana SM, Yao Y, et al. Evaluation of mutational testing of preneoplastic Barrett's mucosa by next-generation sequencing of formalin-fixed, paraffin-embedded endoscopic samples for detection of concurrent dysplasia and adenocarcinoma in Barrett's esophagus. J Mol Diagn 2015;17:412–419.
2. Dulak AM, Stojanov P, Peng S, et al. Exome and whole-genome sequencing of esophageal adenocarcinoma identifies recurrent driver events and mutational complexity. Nat Genet 2013;45:478–486.
3. Sepulveda JL, Komissarova EV, Kongkarnka S, et al. High-resolution genomic alterations in Barrett's metaplasia of patients who progress to esophageal dysplasia and adenocarcinoma. Int J Cancer 2019;145:2754–2766.
4. Shaheen NJ, Falk GW, Iyer PG, et al. Diagnosis and management of Barrett's esophagus: an updated ACG guideline. Am J Gastroenterol 2022;117:559–587.
5. Thrift AP. Global burden and epidemiology of Barrett oesophagus and oesophageal cancer. Nat Rev Gastroenterol Hepatol 2021;18:432–443.
6. Quante M, Bhagat G, Abrams J, et al. Bile acid and inflammation activate gastric cardia stem cells in a mouse model of Barrett's-like metaplasia. Cancer Cell 2012;21:36–51.
7. Kunze B, Middelhoff M, Maurer HC, et al. Notch signaling drives development of Barrett's metaplasia from Dclk1-positive epithelial tuft cells in the murine gastric mucosa. Sci Rep 2021;11:4509.
8. Stachler MD, Taylor-Weiner A, Peng S, et al. Paired exome analysis of Barrett's esophagus and adenocarcinoma. Nat Genet 2015;47:1047–1055.
9. Sherr CJ, Roberts JM. CDK inhibitors: positive and negative regulators of G1-phase progression. Genes Dev 1999;13:1501–1512.
10. Cowan RW, Maitra A. Genetic progression of pancreatic cancer. Cancer J Sudbury Mass 2014;20:80–84.
11. Wang JS, Guo M, Montgomery EA, et al. DNA promoter hypermethylation of p16 and APC predicts neoplastic progression in Barrett's esophagus. Am J Gastroenterol 2009;104:2153–2160.
12. Barrett MT, Sanchez CA, Galipeau PC, et al. Allelic loss of 9p21 and mutation of the CDKN2/p16 gene develop as early lesions during neoplastic progression in Barrett's esophagus. Oncogene 1996;13:1867–1873.
13. Wong DJ, Barrett MT, Stöger R, et al. p16INK4a promoter is hypermethylated at a high frequency in esophageal adenocarcinomas. Cancer Res 1997;57:2619–2622.
14. Sanz-Ortega J, Hernández S, Saez MC, et al. 3p21, 5q21, 9p21 and 17p13.1 allelic deletions are potential markers of individuals with a high risk of developing adenocarcinoma in Barrett's epithelium without dysplasia. Hepatogastroenterology 2003;50:404–407.
15. Klump B, Hsieh CJ, Holzmann K, et al. Hypermethylation of the CDKN2/p16 promoter during neoplastic progression in Barrett's esophagus. Gastroenterology 1998;115:1381–1386.
16. Martin N, Beach D, Gil J. Ageing as developmental decay: insights from p16(INK4a.). Trends Mol Med 2014;20:667–674.
17. Qiu W, Sahin F, Iacobuzio-Donahue CA, et al. Disruption of p16 and activation of Kras in pancreas increase ductal adenocarcinoma formation and metastasis in vivo. Oncotarget 2011;2:862–873.
18. Burd CE, Sorrentino JA, Clark KS, et al. Monitoring tumorigenesis and senescence in vivo with a p16INK4a-Luciferase model. Cell 2013;152:340–351.
19. Ulgen E, Ozisik O, Sezerman OU. pathfindR: an R package for comprehensive identification of enriched pathways in omics data through active subnetworks. Front Genet 2019;10:858.
20. Galiana C, Lozano J-C, Bancel B, et al. High frequency of ki-ras amplification and p53 gene mutations in adenocarcinomas of the human esophagus. Mol Carcinog 1995;14:286–293.
21. Madison R, Chao J, Ross JS, et al. KRAS amplification and mutation are independent events in gastroesophageal adenocarcinomas (GEA). J Clin Oncol 2019;37,70–70.

22. Li J, Poi MJ, Tsai M-D. The regulatory mechanisms of tumor suppressor P16INK4A and relevance to cancer. Biochemistry 2011;50:5566–5582.
23. Kumari R, Jat P. Mechanisms of cellular senescence: cell cycle arrest and senescence associated secretory phenotype. Front Cell Dev Biol 2021;9:645593.
24. Lin AW, Barradas M, Stone JC, et al. Premature senescence involving p53 and p16 is activated in response to constitutive MEK/MAPK mitogenic signaling. Genes Dev 1998;12:3008–3019.
25. Madisen L, Zwingman TA, Sunkin SM, et al. A robust and high-throughput Cre reporting and characterization system for the whole mouse brain. Nat Neurosci 2010; 13:133–140.
26. Barker N, van Es JH, Kuipers J, et al. Identification of stem cells in small intestine and colon by marker gene Lgr5. Nature 2007;449:1003–1007.
27. Tuveson DA, Shaw AT, Willis NA, et al. Endogenous oncogenic K-rasG12D stimulates proliferation and widespread neoplastic and developmental defects. Cancer Cell 2004;5:375–387.
28. Pastuła A, Middelhoff M, Brandtner A, et al. Three-dimensional gastrointestinal organoid culture in combination with nerves or fibroblasts: a method to characterize the gastrointestinal stem cell niche. Stem Cells Int 2016;2016:1–16.
29. Dobin A, Davis CA, Schlesinger F, et al. STAR: ultrafast universal RNA-seq aligner. Bioinformatics 2013;29:15–21.
30. Thorvaldsdóttir H, Robinson JT, Mesirov JP. Integrative Genomics Viewer (IGV): high-performance genomics data visualization and exploration. Brief Bioinform 2013; 14:178–192.
31. Patil I. Visualizations with statistical details: the "ggstatsplot" approach. J Open Source Softw 2021;6:3167.
32. Benjamini Y, Hochberg Y. Controlling the false discovery rate: a practical and powerful approach to multiple testing. J R Stat Soc Ser B Methodol 1995;57:289–300.
33. Venables WN, Ripley BD, Venables WN. Modern applied statistics with S. 4th ed. New York: Springer, 2002.
34. Yu J, Cliften PF, Juehne TI, et al. Multi-platform assessment of transcriptional profiling technologies utilizing a precise probe mapping methodology. BMC Genomics 2015;16:710.
35. Lo K, Gottardo R. Flexible empirical Bayes models for differential gene expression. Bioinforma Oxf Engl 2007; 23:328–335.
36. Bray NL, Pimentel H, Melsted P, et al. Near-optimal probabilistic RNA-seq quantification. Nat Biotechnol 2016;34:525–527.
37. Pimentel H, Bray NL, Puente S, et al. Differential analysis of RNA-seq incorporating quantification uncertainty. Nat Methods 2017;14:687–690.
38. Hao Y, Hao S, Andersen-Nissen E, et al. Integrated analysis of multimodal single-cell data. Cell 2021; 184:3573–3587.
39. Bais AS, Kostka D. scds: computational annotation of doublets in single-cell RNA sequencing data. Bioinformatics 2020;36:1150–1158.
40. Hafemeister C, Satija R. Normalization and variance stabilization of single-cell RNA-seq data using regularized negative binomial regression. Genome Biol 2019;20:296.
41. Zappia L, Oshlack A. Clustering trees: a visualization for evaluating clusterings at multiple resolutions. GigaScience 2018;7:giy083.
42. Squair JW, Gautier M, Kathe C, et al. Confronting false discoveries in single-cell differential expression. Nat Commun 2021;12:5692.
43. Alquicira-Hernandez J, Powell JE. *Nebulosa* recovers single-cell gene expression signals by kernel density estimation. Bioinformatics 2021;37:2485–2487.
44. Martens M, Ammar A, Riutta A, et al. WikiPathways: connecting communities. Nucleic Acids Res 2021; 49:D613–D621.
45. Liberzon A, Birger C, Thorvaldsdóttir H, et al. The Molecular Signatures Database (MSigDB) hallmark gene set collection. Cell Syst 2015;1:417–425.

Received May 1, 2023. Accepted January 22, 2024.

Correspondence
Address correspondence to: Antonia R. Sepulveda, MD, PhD, Department of Pathology, George Washington University, 2300 M Street NW, Suite 712, Washington, DC 20037. e-mail: asepulveda@mfa.gwu.edu.

CRediT Authorship Contributions

Jing Sun, PhD (Investigation: Lead; Methodology: Lead; Visualization: Supporting; Writing – review & editing: Supporting)

Jorge Lemos Sepulveda, MD, PhD (Conceptualization: Supporting; Data curation: Lead; Formal analysis: Supporting; Software: Lead; Visualization: Lead; Writing – original draft: Supporting; Writing – review & editing: Supporting)

Elena V. Komissarova, PhD (Investigation: Supporting; Methodology: Equal; Project administration: Equal; Resources: Supporting; Supervision: Supporting; Validation: Supporting; Writing – review & editing: Supporting)

Caitlin Hills, MD (Investigation: Supporting; Project administration: Supporting; Resources: Supporting; Writing – review & editing: Supporting)

Tyler Seckar, BS (Investigation: Supporting; Writing – review & editing: Supporting)

Narine M. LeFevre, MD (Investigation: Supporting; Writing – review & editing: Supporting)

Hayk Simonyan, MD (Investigation: Supporting; Writing – review & editing: Supporting)

Colin Young, PhD (Supervision: Supporting; Writing – review & editing: Supporting)

Gloria H. Su, PhD (Methodology: Supporting; Resources: Supporting; Writing – review & editing: Supporting)

Armando Del Portillo, MD, PhD (Investigation: Supporting; Writing – review & editing Supporting)

Timothy C. Wang, MD (Resources: Supporting; Writing – review & editing: Supporting)

Antonia R. Sepulveda, MD, PhD (Conceptualization: Lead; Formal analysis: Supporting; Funding acquisition: Lead; Investigation: Supporting; Methodology: Supporting; Project administration: Lead; Resources: Lead; Supervision: Lead; Writing – original draft: Lead; Writing – review & editing: Lead)

Conflicts of interest
The authors disclose no conflicts.

Funding
Supported by R01CA208711 (to A.R.S.).